ARCHIVES OF ELECTRICAL ENGINEERING VOL. 72(4), pp. 951–969 (2023)

DOI 10.24425/aee.2023.147420

Characteristics simulations of the electrodynamic railgun different constructions and their measurement verification

PAWEŁ PIEKIELNY, BRONISŁAW TOMCZUK, ANDRZEJ WAINDOK ✉

Department of Electrical Engineering and Mechatronics
Opole University of Technology
Prószkowska 76 str., 45-758 Opole, Poland
e-mail: {p.piekielny/b.tomczuk/✉a.waindok}@po.edu.pl

(Received: 23.06.2023, revised: 27.07.2023)

Abstract: Dynamic characteristics for three types of railgun constructions were simulated and measured in this work. The simplest construction is the iron-less (IL) railgun, while the two other ones (IC and ICPM) have an iron-core. The iron-core permanent magnet (ICPM) railgun additionally has permanent magnets. To compare their characteristics, similar dimensions of the rails and iron cores were adopted, and the same power supply system was used. Numerical magnetic field analyses and our analytical models have been used to determine the electromagnetic parameters. They were verified experimentally. The transient states of the railguns were studied with our field-circuit mathematical model, and their results were also verified by experiments.

Key words: 3D field analysis, analysis of transients, analytical models, electrodynamic accelerators, experimental verification, field-circuit modeling, projectile velocity

1. Introduction

The research on the electrodynamic accelerators (EA), commonly called railguns, concern mainly military applications and exploration of the space [1–4]. However, more and more studies are related to their applications in industry or measuring systems, like the impact testing of some materials [5–9]. Constructions of accelerators and their power supply systems are being tested [10], as well.

For both military and industrial applications, the main research purpose is the increase the efficiency of the whole system with an accelerator and its power supply. It applies to electromagnetic force and energy amounts and the projectile (bullet, missile) velocity. One of the elements

of research is the active control of the projectile casing (muzzle) velocity [11, 12]. The second one is the bullet energy increasing. For example, in the case of impact tests of materials, it is necessary to determine and raise the impact energy.

One method of expanding EA systems is increasing the power in the accelerator power supply system. The second way of improving the systems is increasing the magnetic flux density value in the projectile area through a geometry modification [13–15]. Thus, the prediction of the projectile energy, based on the parameters of the power supply system, mass and geometry of the projectile, is very important. This can be achieved by an appropriately formulated computational model of the accelerator. The advantage of this approach is the ability to optimize the entire railgun system at the design stage without performing costly prototype tests. In the paper, calculation, and measurement results for three different constructions of relatively small railguns (rail length of 300 mm) were analyzed and compared. The investigated constructions are: an iron-less railgun (IL), iron-core railgun (IC), and iron-core railgun with permanent magnet support (ICPM). Our power supply system consists mainly of a battery of capacitors, which is unloaded through a switch on the thyristor.

2. Physical models

An outline of the investigated iron-less (IL) accelerator construction is given in Fig. 1. The IL structure, which is the simplest construction, was chosen as the basic one – it is used as a reference for comparative analysis of the investigated accelerators. All of the constructions have been designed using analytical and numerical (finite element method – FEM) methods.

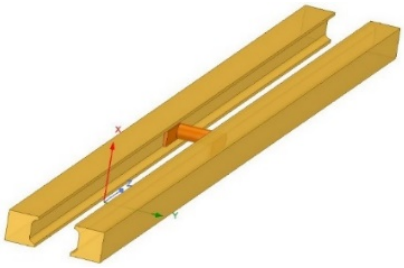

Fig. 1. 3D outline of iron-less (IL) accelerator

The ferromagnetic cores (Figs. 2(a) and 2(b)) were used in order to focus the magnetic field lines in the projectile area [16]. In the case of the ICPM construction, permanent magnets as an additional source of a magnetic field (NdFeB) were implemented [17], (Figs. 2(c) and 2(d)).

For all analyzed constructions of the electrodynamic accelerator, the main dimensions of the brass rails and the projectile were kept constant – the cross section of each rail is 85.8 mm^2. The distance between the rails is $d = 12$ mm, length of the device equals to $l = 300$ mm. Our research was conducted for two types of projectile core material: polytetrafluoroethylene (PTFE) with the trade name Teflon (projectile no. 1), and polyethylene (projectile no. 2). The active part of the projectile is made from an oxygen-free copper (OFC) wire (Fig. 3).

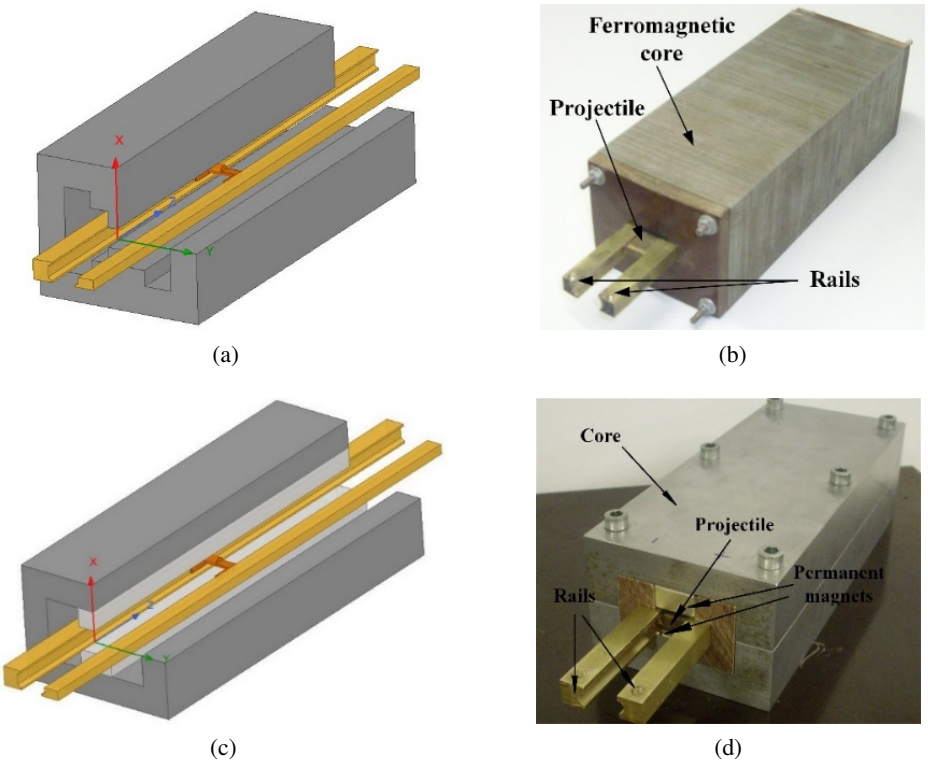

(a) (b)

(c) (d)

Fig. 2. The outlines and pictures of: IC (a), (b); ICPM (c), (d)

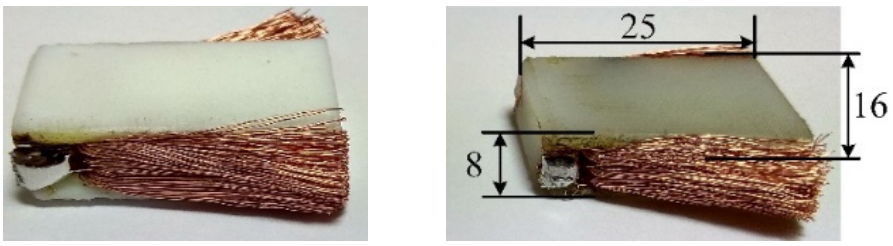

(a) (b)

Fig. 3. Picture of the projectiles (dimensions in mm): no. 1 (m_1 = 7.2 g) (a); no. 2 (m_2 = 5.15 g) (b)

3. Mathematical models

Three different classes of mathematical models were developed for the analysis of the railgun constructions. The first one concerns an analytical model – which allows one to make an initial design of the railgun. The second one concerns modelling with the finite element method (FEM) – for the precise calculation of railgun differential and integral parameters of the electromagnetic field [18]. The third one deals with a field-circuit model of the actuator transients.

3.1. Analytical models of the accelerators

In the initial engineering phase of the iron-less (IL) accelerator, analytical models were used. For the IL design, the model based on the Biot-Savart law was used to calculate the magnetic field distribution in the projectile area and its thrust force. Using the denotations from Fig. 4, the following expression for the magnetic field density produced by one rail was obtained:

$$B(y_P) = \frac{\mu_0 \cdot I}{4\pi y_p} \cdot \left(\frac{l}{\sqrt{l^2 + y_P^2}} \right). \tag{1}$$

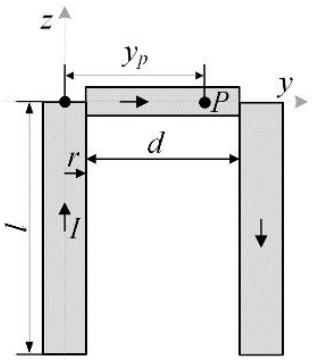

Fig. 4. Simplified model of the iron-less rail accelrator

The Lorentz force acting on the projectile (in z direction) is described by the following integral:

$$\vec{F} = \int_{w_s}^{w_s+d} \mathrm{d}\vec{F}(y) = \int_{w_s}^{w_s+d} IB(y)\,\mathrm{d}y. \tag{2}$$

The integration of magnetic flux density function $B(y)$ is carried out along the length of the projectile in the y direction. After the integral (2) calculation, and taking into account two rails, the following expression for the force is obtained:

$$F = \frac{\mu_0 \cdot I^2}{2\pi} \left(\ln\left(\frac{l + \sqrt{l^2 + w_s^2}}{r} \right) - \ln\left(\frac{l + \sqrt{l^2 + (w_s + d)^2}}{w_s + d} \right) \right). \tag{3}$$

In the case of construction with a ferromagnetic core, the analytical model is based on the reluctance network created for the accelerator's individual parts (Fig. 5(a)). The symmetry of the object was taken into account in the calculations, as well.

Due to a high-leakage magnetic field in the air gap area, the reluctance value for all leakage flux lines was taken into account (Fig. 6). The total reluctance value for the air gap was calculated

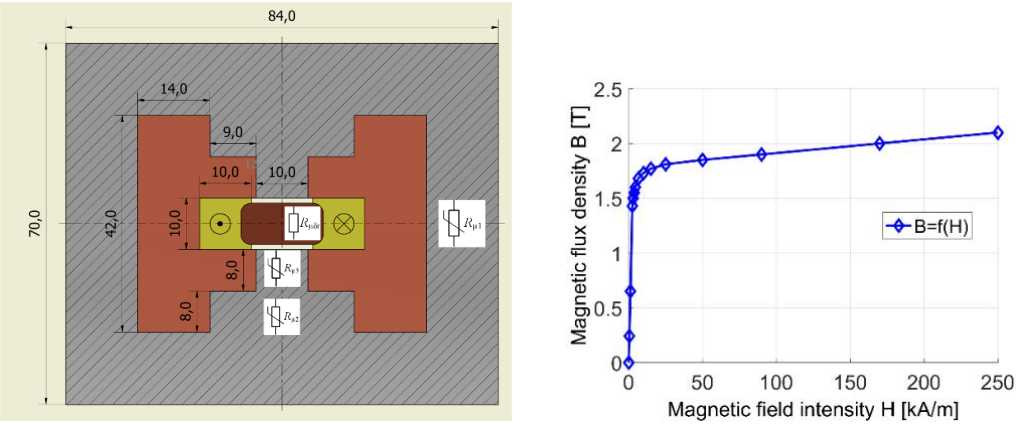

(a) (b)

Fig. 5. IC accelerator cross-section (a); measured B/H curve for the ferromagnetic core (b)

using the following expression:

$$R_{\mu\delta r} = \frac{\dfrac{\delta}{\mu_0 \cdot 0.01 \cdot l} \cdot \dfrac{0.17 \cdot \delta + 0.14 \cdot h_t}{\mu_0 \cdot l \cdot h_t}}{\dfrac{\delta}{\mu_0 \cdot 0.01 \cdot l} + \dfrac{0.17 \cdot \delta + 0.14 \cdot h_t}{\mu_0 \cdot l \cdot h_t}} = 8.385 \cdot 10^6 \ 1/\mathrm{H}, \tag{4}$$

where: δ is the air gap length, h_t represents the leakage flux lines high on the lateral surface of the pole, (Fig. 6).

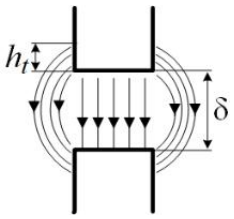

Fig. 6. Main and leakage magnetic flux in the air gap

Taking into account the non-linear B/H curve (Fig. 5(b)), in order to obtain the magnetic flux value Φ in the air gap (Fig. 5(a)) the following non-linear equation was solved:

$$I - R_{\mu\delta r}\Phi = \left(R_{\mu 1}(\Phi) + 2R_{\mu 2}(\Phi) + 2R_{\mu 3}(\Phi)\right) \cdot \Phi. \tag{5}$$

Assuming the magnetic flux density and current intensity vectors, which are perpendicular to each other, Lorentz's force was determined:

$$\vec{F} = \vec{B} \times \vec{I} \cdot w_b \,, \tag{6}$$

where: w_b is the width of the projectile, $\vec{B}$ is the average value of the magnetic flux density in the projectile obtained from the flux calculation (Eq. (5)).

In the case of the ICPM accelerator, the reluctance model was used, as well. In this case, an additional source of the magnetic field was included (permanent magnets) (Fig. 7(a)). Due to the relatively large width of the magnets, the analytical model for the ICPM did not include the effect of magnetic flux leakage in the air gap.

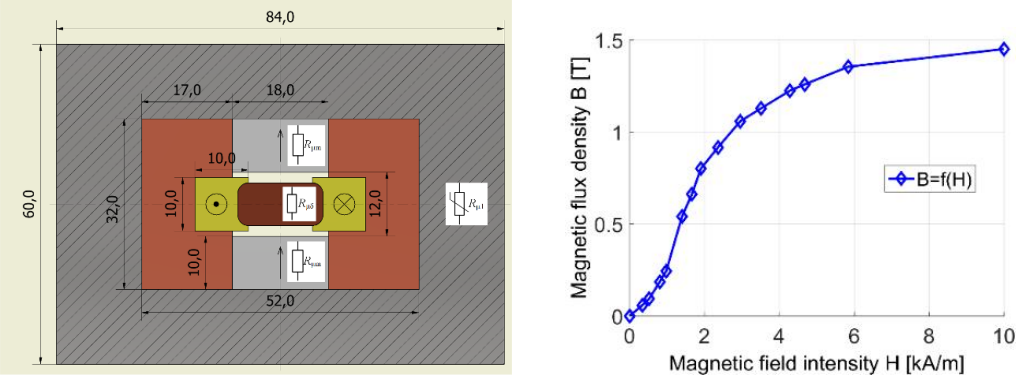

(a) (b)

Fig. 7. ICPM accelerator: cross-section (a); measured B/H curve of the solid steel ferromagnetic core (b)

For such a construction (Fig. 7(a)), the non-linear equation concerning the magnetic flux takes the following form:

$$R_{\mu 1}(\Phi) \cdot \Phi = I + 2H_c \cdot h - R_{\mu\delta}\Phi - 2R_{\mu m}\Phi. \tag{7}$$

In Table 1, the parameters necessary for solving Eqs. (5) and (7), are given.

Table 1. Reluctance values for linear parts of the magnetic circuit for ICPM and IC

ICPM			**IC**
H_c **[kA/m]**	h_m **[m]**	$R_{\mu\delta}$ **[1/H]**	$R_{\mu\delta r}$ **[1/H]**
890	0.01	$5.305 \cdot 10^6$	$8.385 \cdot 10^6$

3.2. Numerical models of the accelerators

In the pursuit of interactive design, we tried to reduce the computation time to a minimum. We tested that for the investigated accelerators (Figs. 1 and 2), with a relatively small cross-section of the rails (buss-bars), the eddy currents have no decisive impact on the bullet dynamics. Therefore, instead of the difficult solving of partial differential equations (PDEs) with a time variable, we used the field-circuit model of three actuators [19, 20]. The calculations were divided into two parts of execution. Part 1 concerns the prediction of electromagnetic parameters, which are the so-called integral parameters of the field analysis, whereas in part 2, the field-circuit method has been applied to the transient analysis of the three constructions of railgun. The numerical analyses of the 3D magnetic field have been carried out using a magnetostatic module in the Ansys-Maxwell software which is based on the finite element method – FEM, [13].

To predict the electrodynamic force in the three constructions, we omitted the eddy currents in iron parts, but due to their magnetic saturation we included the $B-H$ curve in the magnetostatic model. The $\vec{T}-\phi$ formulation has been used for 3D magnetic field analysis. In such a case, the magnetic field H is represented in terms of the magnetic scalar potential ϕ and electric vector potential $\vec{T}$:

$$\vec{H} = \vec{T} + \nabla\phi. \tag{8}$$

On the other hand, the magnetic field strength rotation can be expressed as:

$$\nabla \times \vec{H} = \vec{J}_s\,. \tag{9}$$

The current density depends on the electric strength $\vec{E}$ and electrical conductance σ.

$$\vec{J}_s = \sigma\vec{E}. \tag{10}$$

Omitting the eddy currents in the rail gun construction, the rotation of electric field intensity is equal to zero.

$$\nabla \times \vec{E} = 0. \tag{11}$$

Taking into account the above, we can introduce the electric scalar potential V as:

$$\vec{E} = -\nabla V. \tag{12}$$

Including the divergence of the current density vector:

$$\nabla \cdot \vec{J}_s = 0, \tag{13}$$

the following Laplace equation is obtained:

$$-\nabla \cdot (\sigma \nabla V) = 0. \tag{14}$$

The above relationship allows the application of the voltage boundary condition and the determination of the potential distribution along the conductive rails of the accelerator. Knowing the value of the current intensity in the rails and the projectile, we have the possibility to determine the distribution of the magnetic field in the analyzed area. For air and rails, the reduced magnetic scalar potential in the following equation is calculated:

$$\nabla \cdot (\mu_0 \nabla\phi) = -\nabla \cdot \left(\mu_0 \vec{H}_p\right). \tag{15}$$

In a ferromagnetic region, for which $\vec{J}_s = 0$, the homogeneous partial differential equation for the scalar potential is solved:

$$\nabla \cdot (\mu_0 \nabla\phi) = 0. \tag{16}$$

The above relationships allow the application of the voltage boundary condition and the determination of the electric scalar potential distribution along the conductive rails of the accelerator, which in turn allows the determination of the current density distribution.

Based on the obtained distributions of the magnetic and electric fields, their integral parameters can be determined. They are particularly important in the further analysis of transients, which

in this paper were studied using the field-circuit model. The magnetic flux passing through the surface S (bounded by the projectile and rails) is determined as the integral of the scalar product of the magnetic induction vector and the unit normal vector, over the closed surface of this circuit:

$$\Phi_S = \int_S \vec{\boldsymbol{B}} \cdot \vec{\boldsymbol{n}} \, \mathrm{d}S, \tag{17}$$

where: Φ_S is the flux limited by the area S; $\vec{\boldsymbol{B}}$ is the magnetic flux density vector; $\vec{\boldsymbol{n}}$ is the unit vector normal to the surface S.

The second calculated parameter is the total value of the current flowing in the circuit at a given excitation and projectile position.

$$I = \int_S \vec{\boldsymbol{J}} \cdot \vec{\boldsymbol{n}} \, \mathrm{d}S. \tag{18}$$

The Lorentz force F_z acting on the projectile in the exit direction was calculated from the relationship:

$$F_z = \int_{\Omega_m} \boldsymbol{N}^T \left(\vec{\boldsymbol{J}} \times \vec{\boldsymbol{B}} \right) \mathrm{d}\Omega_m \,, \tag{19}$$

where: Ω_m is the projectile volume [m^3]; $\boldsymbol{N}^T$ is the shape function vector.

For the field-circuit model, an important parameter of the accelerator is its dynamic inductance L_d, calculated on the basis of the definition formula, as the partial derivative of the flux Φ_S, associated with the rails in relation to the current:

$$L_d = \frac{\partial \Phi_S}{\partial i} = \frac{1}{i} \frac{\partial W_m}{\partial i} \,. \tag{20}$$

The obtained results from the magnetostatic calculations: force, magnetic flux and dynamic inductance, were parameterized with respect to the excitation current and projectile position.

Three types of boundary conditions have been used: the voltage boundary conditions on the rails ends, tangential and normal conditions for the magnetic flux intensity vector on the symmetry planes of the model (Fig. 8).

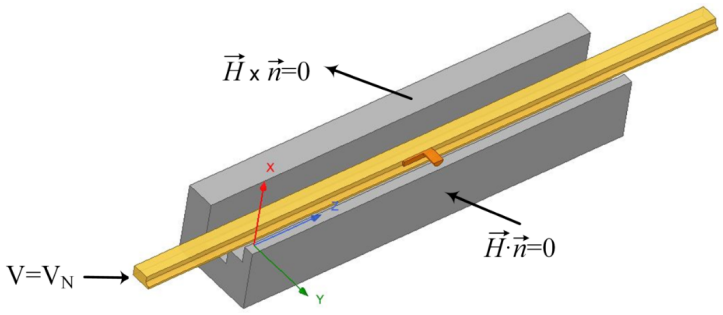

Fig. 8. IC accelerator: boundary conditions

The transient model was obtained based on the Euler-Lagrange method. A system of three equations describing the motion of the projectile and the current intensity waveform (under voltage excitation) was obtained:

$$\frac{\mathrm{d}v}{\mathrm{d}t} = \frac{F(i,z) - Dv - D_p v^2}{m}, \tag{21}$$

$$\frac{\mathrm{d}z}{\mathrm{d}t} = v, \tag{22}$$

$$\frac{\mathrm{d}i}{\mathrm{d}t} = \frac{-Ri - \frac{\mathrm{d}}{\mathrm{d}z}\left(\Phi_s(i,z)\right) v - \frac{q}{C}}{L_d(i,z)}, \tag{23}$$

where: z is the projectile position, v is the projectile velocity, m is the projectile mass, D is the kinetic friction coefficient, D_p is the air friction coefficient, R is the circuit resistance, q is the charge, i is the excitation current, C is the capacitance, $F(i,z)$ is the force, $\Phi_s(i,z)$ is the magnetic flux, $L_d(i,z)$ is the dynamic inductance.

The above equations have been implemented in the Matlab–Simulink software. The block diagram of the model is presented in Fig. 9.

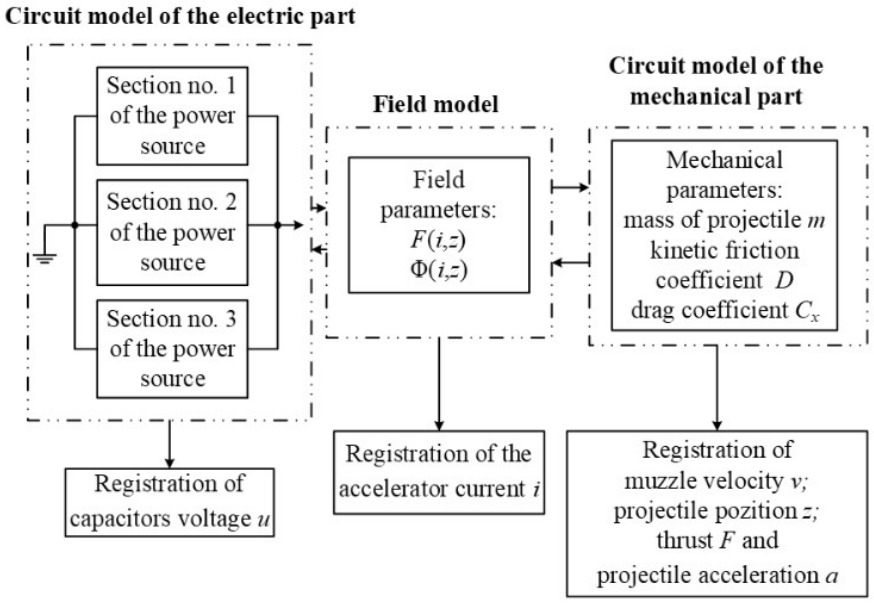

Fig. 9. Block diagram of the field-circuit model

The characteristics obtained from the magnetostatics calculations (force, magnetic flux, and dynamic inductance – see Section 4) were implemented in the form of 3-dimensional tables in the model.

4. Magnetostatic calculation results

In Fig. 10, the values of electrodynamic force for two constructions of accelerators are given. They depend on the maximal excitation current intensity in the rails and approximately increase, according to the exponential function of the current intensity peak values. In the analyzed current intensity value range, the IC construction has slightly higher force values, than the ICPM. However, the IL structure has the worst characteristics.

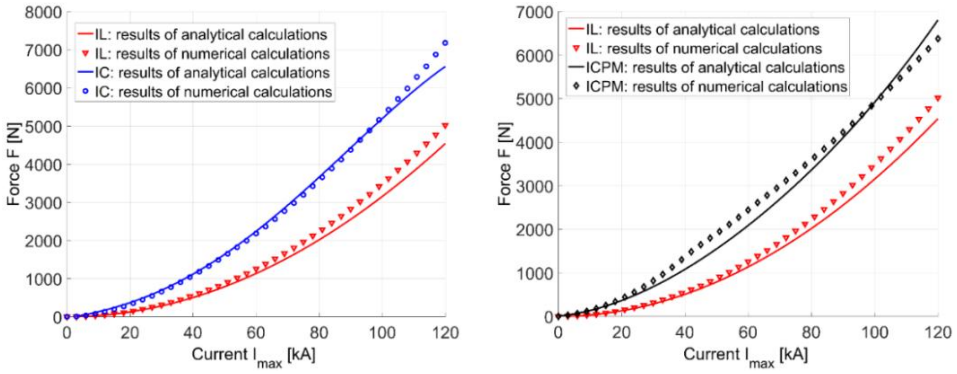

(a) (b)

Fig. 10. Force vs. maximum value of excitatin current for different mathematical models and accelerator constructions: (a) IC vs IL; (b) ICPM vs IL

A good conformity between analytical and numerical calculation results was obtained, which confirms the correctness of the developed mathematical models. Thus, both analytical and numerical models could be used for the prediction of the electromagnetic characteristics, which have to be used in the field-circuit model.

The magnetic flux density distributions have been obtained using an FEM model. For example, when the projectile is in the middle of the rails in which the current intensity amounts to $I = 60$ kA, the distribution of B is presented in Fig. 11. For IC construction, the highest (about 6 T) value of the magnetic flux is observed in the projectile area.

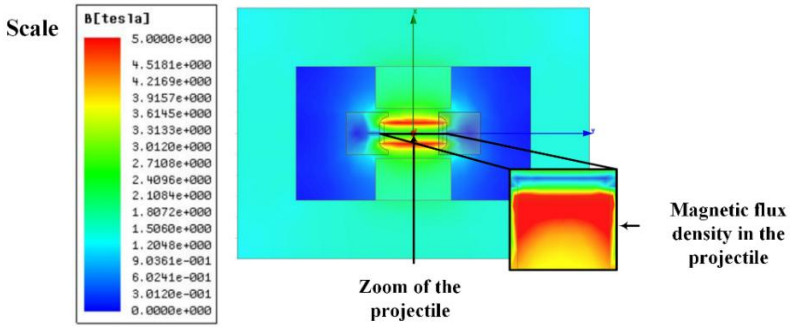

(a)

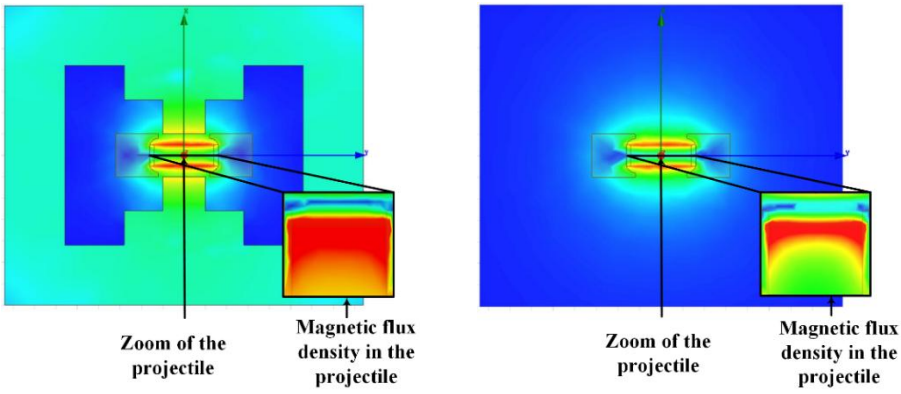

(b) (c)

Fig. 11. Magnetic flux density distribution in the cross-section of the accelerator and projectile for I = 60 kA: ICPM (a); IC (b); IL (c)

It is possible to determine integral parameters of the field and then electromagnetic parameters of the accelerator. The parameters are particularly important in the analysis of the transients, which have been analyzed using our field-circuit method. For the purpose of the transient simulations, a series of calculations for different values of the excitation current intensities at a variable position of the projectile were carried out. The result of the calculations are the characteristics of force and flux vs. the projectile position and excitation current I (Figs. 12 and 13).

From the characteristics of force vs. projectile positions and excitation current values, it can be concluded that the use of a ferromagnetic core results in an increase in the thrust force value of almost 43%. In the case of the IL accelerator, the change in the position of the projectile has a small effect on the obtained force. Only for the end-positions of the projectile a drop in the force value is visible (Fig. 12(a)). However, in the case of the railgun with a ferromagnetic core, the drop of the force value after the projectile reaches the position of 250 mm is observed in Figs. 12(b), and 12(c). This is due to the shorter length of the core in relation to the rails, where the segment lengths of 50 mm in the rails are not surrounded by the iron core. The magnetic

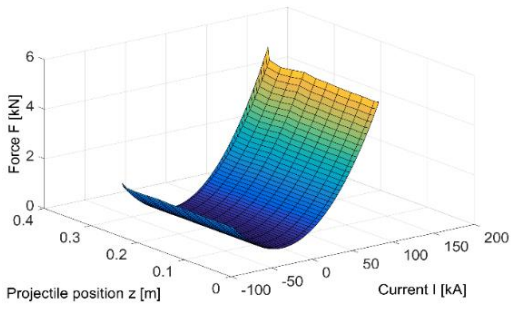

(a)

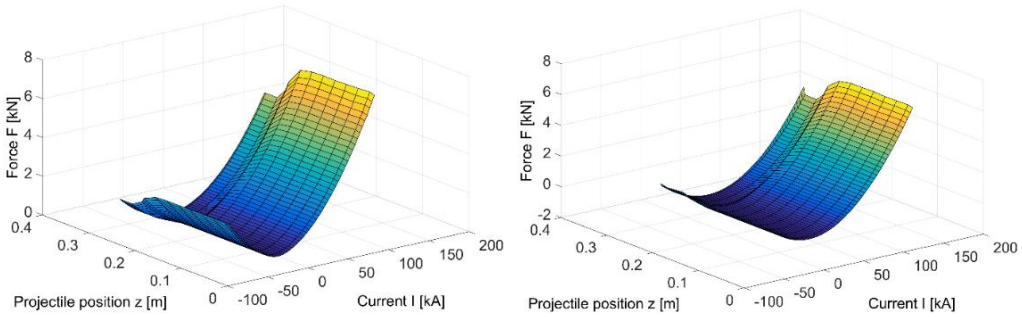

(b) (c)

Fig. 12. Thrust force vs. rails current intensity and projectile position for: IL (a); IC (b); ICPM (c)

flux value depends strongly on both the projectile position and excitation current intensity values (Fig. 13).

The increase of the magnetic flux vs. position is practically linear – it is due to the nearly linear dependence of the magnetic flux vs. projectile position, which determines the integration surface. The end effect is visible in the case of the IC accelerator (Fig. 13(b)) – for the rail segments not

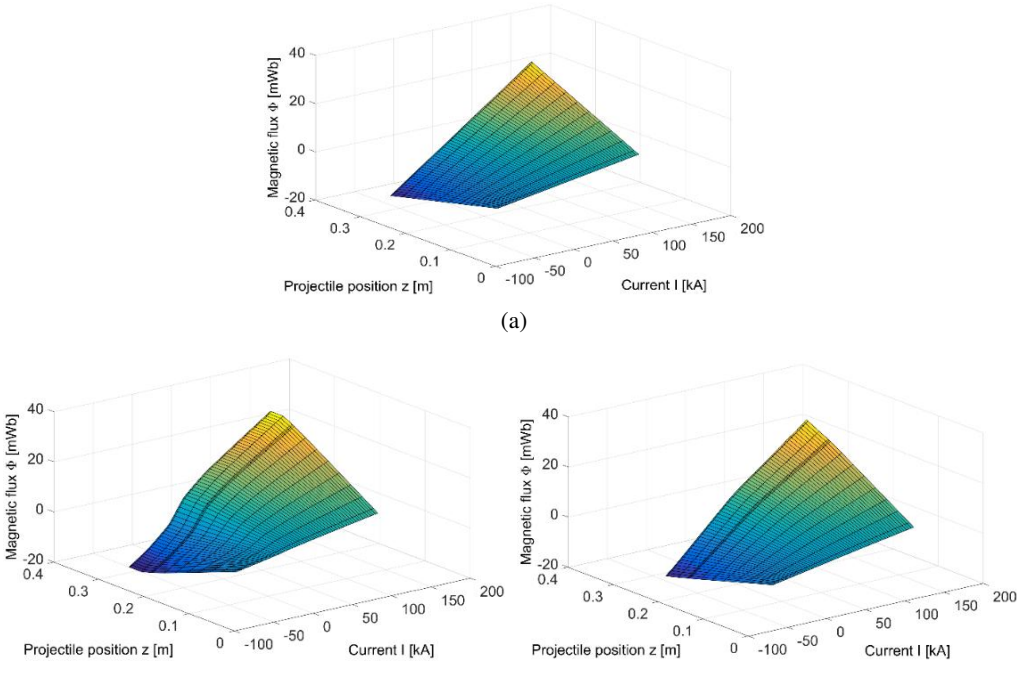

(a)

(b) (c)

Fig. 13. Magnetic flux quantity vs current intensity value and projectile position for: IL (a); IC (b); ICPM (c)

surrounded by the iron core, the magnetic flux increases slower vs. the projectile position. The increase of the magnetic flux vs. current values is linear only in the case of the IL construction (Fig. 13(a)) – for the constructions with an iron core, the influence of the nonlinear B/H curve is visible (Figs. 13(b) and 13(c)).

5. Transient calculations and measurement results

The transients of the accelerators were verified experimentally for different values of initial capacitor voltage. The same three-section capacitor bank in the power supply system was used for each event. It should be emphasized that for the tested accelerator designs a very good measurement recurrence of the excitation current intensity waveforms and voltage on the capacitor banks was obtained. The differences in the measured missile velocity, for the same accelerator construction, did not exceed 1%.

The waveforms of capacitor voltage and the current intensity in the accelerator rails, for all railgun constructions, were also compared at the same supply system settings, as well. In the tests, the projectile core made of polytetrafluoroethylene (Section 2) was used (mass m = 7.2 g). The measurement results are presented in Fig. 14. The voltage and current intensity waveforms are practically identical for the same power supply system.

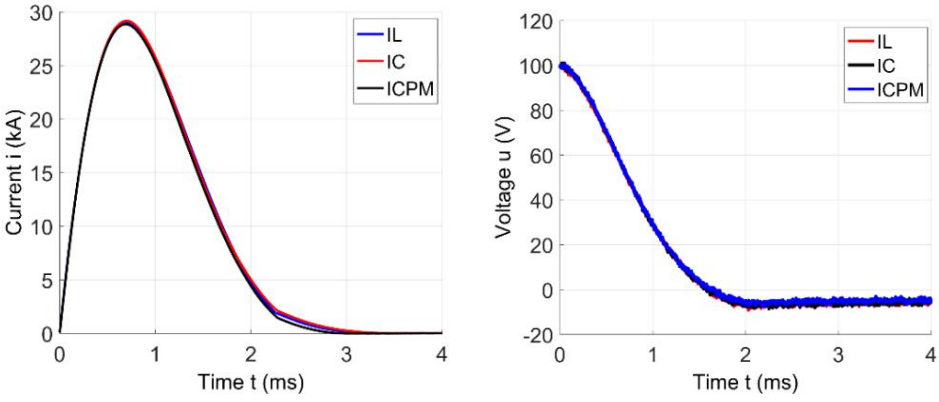

(a) (b)

Fig. 14. Comparison of current and voltage waveforms for the tested rail accelerators (U = 100 V, C = 0.333 F): excitation current waveform (a); capacitor voltage waveform (b)

In Figs. 15–17, an exemplary measurement verification of the field-circuit model, for the IL, IC and ICPM, is presented. In all these cases, the same power voltage supply of the capacitor was assumed, and the capacitor was charged to U = 128 V. A very good conformity between the calculation and measurement results is also observed.

The measurement verification of the projectile velocity was carried out as well (Tables 2 and 3). The use of the ferromagnetic core (IC) increased three times the muzzle velocities (for the low voltage values) in comparison with the iron-less accelerator. For the higher voltage (148 V)

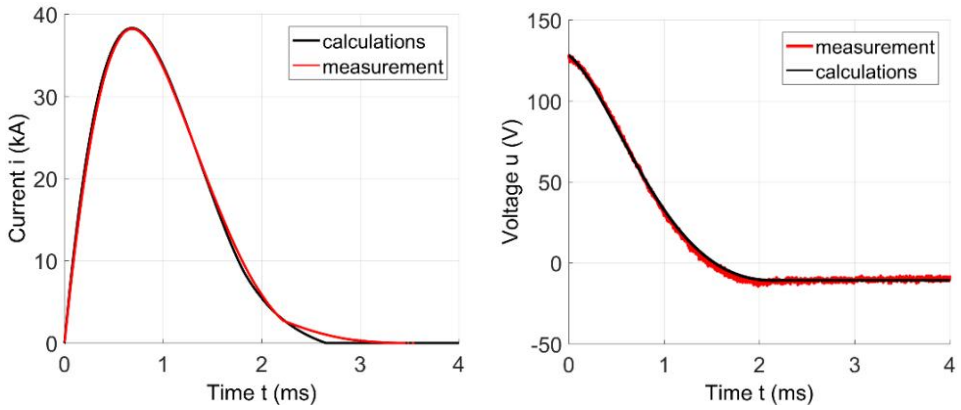

(a) (b)

Fig. 15. The tests of the field-circuit model for the first cunstruction (IL) for U = 128 V: excitation current vs. time (a); voltage waves (b)

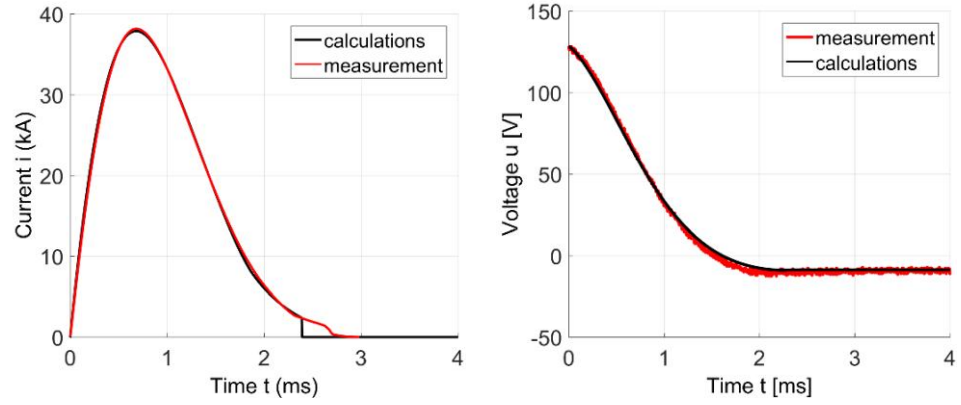

(a) (b)

Fig. 16. Measurement verification of the field-circuit model for the construction with iron magnetic circuit (IC) under excitation voltage U = 128 V: excitation current vs. time (a); voltage waves (b)

that increase was about 150%. A more significant increase in muzzle velocities is visible for a lighter projectile (no. 2). In the case of the ICPM design, the increase in muzzle velocity for the lowest voltage values amounted nearly to 600%. For the highest voltages, 95% higher muzzle velocities were obtained compared to the IL construction. Comparing the IC and ICPM, for the voltage values above 100 V (excitation current value 29.150 kA) better properties are obtained for the IC. It means that for higher current values, the IC construction is a better solution.

The best agreement between the calculation and measurement results was obtained for the projectile no. 1 (the differences do not exceed 3%). The largest discrepancies between the measurement and calculation results can be observed for the ICPM construction.

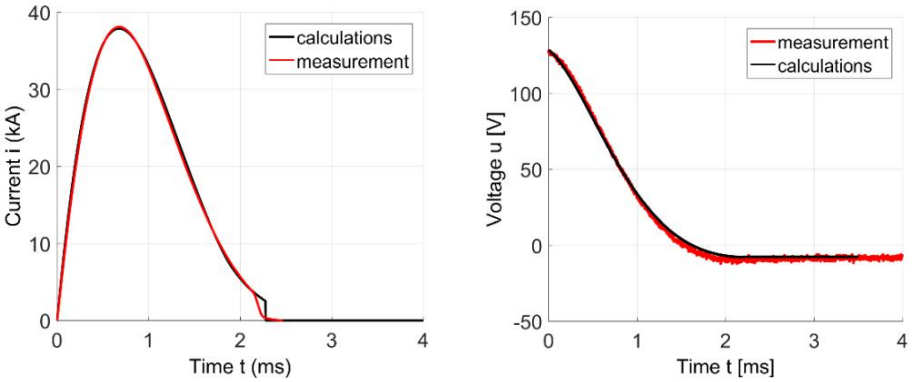

(a) (b)

Fig. 17. Measurement tests of the field-circuit model of the iron magnetic system with permanent magnets (ICPM) for U = 128 V: excitation current vs. time (a); voltage waves (b)

Table 2. Measurement verification of muzzle velocity for projectile no. 1 (Sec. 2)

Voltage	**IL**		**IC**		**ICPM**	
U **[V]**	v_{mes} **[m/s]**	v_{cal} **[m/s]**	v_{mes} **[m/s]**	v_{cal} **[m/s]**	v_{mes} **[m/s]**	v_{cal} **[m/s]**
70	12.79	13.27	39.81	41.91	52.08	54.20
100	32.28	34.47	85.03	83.77	85.62	96.24
128	60.10	62.39	141.24	135.16	123.27	145.16
148	77.16	82.60	179.86	172.72	151.70	176.05

Table 3. Measurement verification of muzzle velocity for projectile no. 2 (Sec. 2)

Voltage	**IL**		**IC**		**ICPM**	
U **[V]**	v_{mes} **[m/s]**	v_{cal} **[m/s]**	v_{mes} **[m/s]**	v_{cal} **[m/s]**	v_{mes} **[m/s]**	v_{cal} **[m/s]**
70	19.53	19.30	56.05	56.64	71.84	75.32
100	46.99	48.08	112.11	114.07	119.28	132.65
128	82.24	84.04	198.41	184.24	166.22	190.57
148	115.21	116.70	277.78	230.10	203.25	232.32

6. Velocity and energy prediction of projectile for different accelerator construction

For practical application of the electrodynamic accelerators, e.g. for strength tests of various materials, an important aspect is to determine the impact energy, as accurately as possible, in a wide range of its changes. Based on our research, it can be concluded that the presented calculation

models are accurate enough to predict the parameters of the constructions, at their design stage. Thus, the prediction of energy and muzzle velocity of the bullet, as well as their power efficiency, has been affected by a wide range of supply voltage values (from 50 V to 500 V).

In Fig. 18(a), the relationship between muzzle velocity and the capacitor system voltage in the IC construction for two different projectiles, is shown. The velocity increases almost exponentially along with the initial voltage, increasing in the range from 50 V to 120 V, whereas for higher voltage values, the relationship is almost linear. In the case of a lighter projectile, the discrepancies between the calculations and measurements are higher and up to 14% for a voltage value of 148 V. In Fig. 18(b), the relationship between projectile energy and the capacitor system voltage is also given.

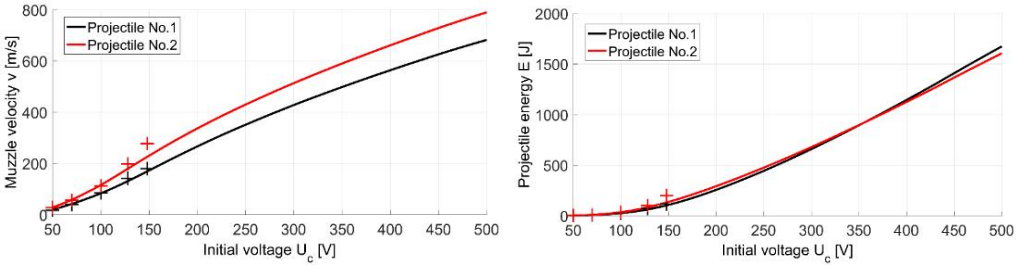

(a) (b)

Fig. 18. Muzzle velocity (a) and projectile energy (b) vs. initial voltage values for IC (measurements are denoted by +)

Projectile no. 2, with a lower mass, achieves higher energy values in comparison with projectile no. 1, for the voltage range from 50 V to 350 V. Above a voltage of 350 V, higher energies are obtained for projectile no. 1. This is most likely caused by the higher impact of losses associated with the friction of a lighter projectile.

Additionally, within the transient state calculations, the dependence of the maximum value of the $I_{\max}$ current vs. the excitation initial voltage was determined (Fig. 19). The value of the Imax current intensity increases almost linearly as a function of the U_c voltage. However, a slight

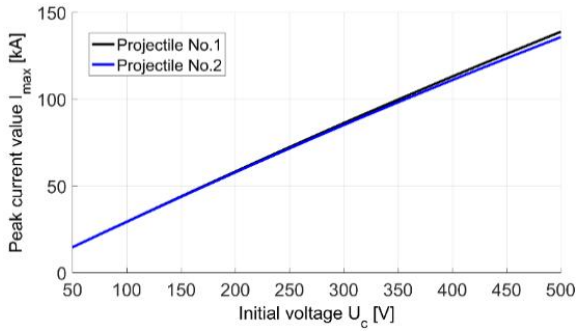

Fig. 19. The calculated value of the maximum current vs. initial voltage

impact of the projectile mass on the peak value of this current is visible – higher values are obtained for projectile no. 1 (heavier missile). This is due to the lower speeds achieved by this projectile in comparison with bullet no. 2. After the same time, bullet no. 1 is closer to the power supply system than bullet no. 2, and due to lower resistance of the rail-projectile circuit the current in the rails is greater.

The efficiency of the accelerators discussed in this work is below 6% and depends slightly on the projectile mass (Figs. 20 to 21). For lower supply voltages (below 350 V), the efficiency is higher in the case of the projectile with lower mass. Above 350 V, in the case of the IC and ICPM, the higher efficiency is observed for the heavier projectile (Fig. 20). In the case of the IL construction, the higher efficiency for the projectile with higher mass is observed above 500 V (Fig. 21(a)).

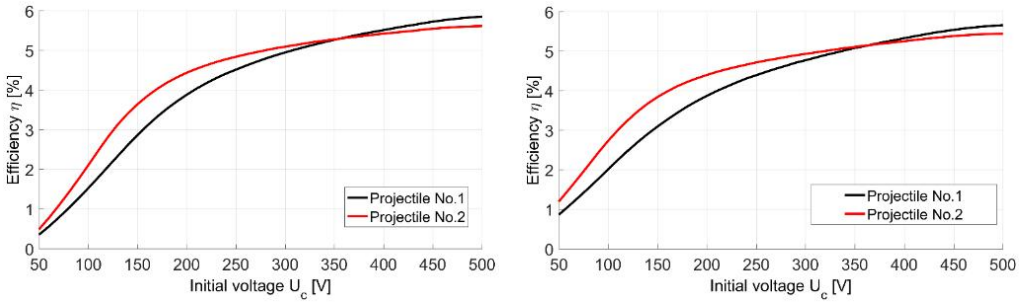

(a) (b)

Fig. 20. Efficiency vs. capacitor initial voltage for: (a) IC; (b) ICPM

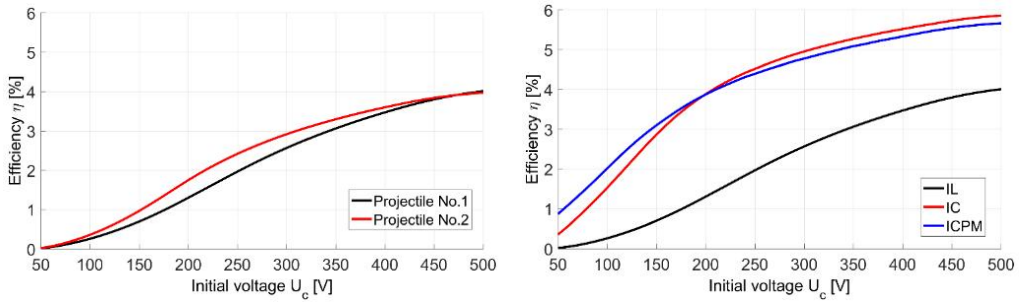

(a) (b)

Fig. 21. Efficiency vs. capacitor initial voltage for: (a) IL and two different projectiles; (b) different railgun contructions (projectile no. 1)

The efficiency depends nonlinearly vs. supply voltage. For lower capacitor voltage values, it increases more significantly than for the higher ones (it looks like the saturation of efficiency value). For voltages below 200 V, the highest efficiency is observed in the ICPM construction, while above the 200 V the IC construction is better (Fig. 21(b)). However, the differences are not significant. The worst efficiency is observed in the case of the IL construction.

7. Conclusions

Dynamic characteristics for three types of railgun constructions were simulated and measured in this work. To further speed up the calculations using our field-circuit model, the electromagnetic parameters were previously calculated and tabulated as functions of current intensity and the projectile displacement.

In the initial phase of rail accelerator design, it is reasonable to use an analytical model to calculate the bullet electrodynamic force. A good agreement between the results obtained with our analytical model and those from the 3-D magnetic field analysis confirms the correctness of the developed analytical model for the determination of static characteristics.

In order to increase energy through magnetic circuit improvement, a 3-D electromagnetic field analysis had to be performed and integral parameters of this field determined. The obtained distributions of magnetic and electric fields allow one to determine their integral parameters, e.g. the magnetic flux passing through the surface bounded by the projectile and rails, and thus the inductance of the above-mentioned circuit. For the fixed geometrical dimensions of the accelerator, a slight increase in the mass of the projectile has almost no effect on the electromagnetic parameters.

The presented constructions with an iron-core (IC) and permanent magnets (ICPM) allow for increasing the efficiency of the entire system in relation to the base air structure (IL). The largest increase of muzzle velocity was observed for the lowest initial voltages of the capacitor bank. For higher voltage values at increased current intensity, the core saturation effects decrease the benefits of the ferromagnetic core applied.

Comparing the obtained projectile energies for the IC and ICPM constructions, it should be noticed that for smaller excitation current values the ICPM structure is better, while above the saturation point of the core material, the IC is characterized by better parameters. It is due to the fact that after exceeding the saturation point of the core material, magnets in the ICPM structure create an additional reluctance for the magnetic flux.

In this work, the parameters of the rail-gun systems were determined and verified by measurements. For higher supply voltages, the higher energy is observed, and the better efficiency is obtained for heavier projectiles. However, the change of the projectile mass only slightly influences the accelerator parameters.

References

[1] Hundertmark S., Vincent G., Schubert F., Urban J., *The NGL-60 Railgun*, IEEE Transactions on Plasma Science, vol. 47, no. 7, pp. 3327–3330 (2019), DOI: 10.1109/TPS.2019.2921099.

[2] Hundertmark S., Lancelle D., *A Scenario for a Future European Shipboard Railgun*, IEEE Transactions on Plasma Science, vol. 43, no. 5, pp. 1194–1197 (2015), DOI: 10.1109/TPS.2015.2403863.

[3] Gallant J., Vancaeyzeele T., Lauwens B., Wild B., Alouahabi F., Schneider M., *Design considerations for an electromagnetic railgun firing intelligent bursts to be used against antiship missiles*, IEEE Transactions on Plasma Science, vol. 43, no. 5, pp. 1179–1184 (2015), DOI: 10.1109/TPS.2015.2416774.

[4] Lehmann P., Reck B., Vo M.D., Behrens J., *Acceleration of a Suborbital Payload Using an Electromagnetic Railgun*, IEEE Transactions on Magnetics, vol. 43, no. 1, pp. 480–485 (2007), DOI: 10.1109/TMAG.2006.887666.

[5] Siemenn A.E., Deo B., Ng F., Zhou J., Owens C., Atue S.U., Forsuelo M., *A Railgun Secondary Propulsion System for High-Speed Hyperloop Transportation*, IEEE Transactions on Plasma Science, vol. 51, no. 1, pp. 243–248 (2023), DOI: 10.1109/TPS.2022.3232406.

[6] Gores P.A., Vincent G., Schneider M., Spray J.G., *Appraisal of Rapid-Fire Electromagnetic Launch Effects on Ceramic Targets*, IEEE Transactions on Plasma Science, vol. 47, no. 8, pp. 4175–4180 (2019), DOI: 10.1109/TPS.2019.2921731.

[7] Vricella A., Delfini A., Pacciani A., Pastore R., Micheli D., Rubini G., Marchetti M., Santoni F., *A new advanced railgun system for debris impact study*, Procedia Structural Integrity, vol. 3, pp. 545–552 (2017), DOI: 10.1016/j.prostr.2017.04.044.

[8] Poniaev S.A., Bobashev S.V., Zhukov R.O., Sedov A.I., Izotov S.N., Kulakov S.L., Smirnova M.N., *Small-size railgun of mm-size solid bodies for hypervelocity material testing*, Acta Astronautica, vol. 109, pp. 162–165 (2015), DOI: 10.1016/j.actaastro.2014.11.012.

[9] Schneider M., Vincent G., Hogan J.D., Spray J.G., *The use of a railgun facility for dynamic fracture of brittle materials*, IEEE Transactions on Plasma Science, vol. 43, no. 5, pp. 1162–1166 (2015), DOI: 10.1109/TPS.2015.2396081.

[10] Guo X., Dai L., Zhang Q., Lin F., Huang Q., Zhao T., *Influences of Electric Parameters of Pulsed Power Supply on Electromagnetic Railgun System*, IEEE Transactions on Plasma Science, vol. 43, no. 9, pp. 3260–3267 (2015), DOI: 10.1109/TPS.2014.2349997.

[11] Chang X., Yu X., Liu X., Li Z., He H., *A Closed-Loop Velocity Control System for Electromagnetic Railguns*, IEEE Transactions on Plasma Science, vol. 47, no. 5, pp. 2269–2274 (2019), DOI: 10.1109/TPS.2018.2879798.

[12] Siaenen T., Schneider M., Zacharias P., Löffler M.J., *Actively Controlling the Muzzle Velocity of a Railgun*, IEEE Transactions on Plasma Science, vol. 41, no. 5, pp. 1514–1519 (2013), DOI: 10.1109/TPS.2013.2245672.

[13] Waindok A., Piekielny P., *Analysis of an iron-core and ironless railguns powered sequentially*, Compel, vol. 37, no. 5, pp. 1707–1721 (2018), DOI: 10.1108/COMPEL-12-2017-0533.

[14] Vincent G., Hundertmark S., *Using the SR\3–60 Railgun in Augmented Mode*, IEEE Transactions on Plasma Science, vol. 43, no. 5, pp. 1555–1558 (2015), DOI: 10.1109/TPS.2015.2405572.

[15] Jin L., Lei B., Zhang Q., Zhu R., *Electromechanical Performance of Rails with Different Cross-Sectional Shapes in Railgun*, IEEE Transactions on Plasma Science, vol. 43, no. 5, pp. 1220–1224 (2015), DOI: 10.1109/TPS.2015.2413892.

[16] Piekielny P., Waindok A., *Transient Analysis of a Railgun with Iron Core*, Przegląd Elektrotechniczny, vol. 93, no. 2, pp. 152–155 (2017), DOI: 10.15199/48.2017.02.33.

[17] Waindok A., Piekielny P., *Transient Analysis of a Railgun with Permanent Magnets Support*, Acta Mechanica et Automatica, vol. 11, no. 4, pp. 302–307 (2017), DOI: 10.1515/ama-2017-0046.

[18] Tomczuk B., Koteras D., *Magnetic Flux Distribution in the Amorphous Modular Transformers*, Journal of Magnetism and Magnetic Materials, vol. 323, no. 12, pp. 1611–1615 (2011), DOI: 10.1016/j.jmmm.2011.01.007.

[19] Wajnert D., Sykulski J.K., Tomczuk B., *An Enhanced Dynamic Simulation Model of a Hybrid Magnetic Bearing Taking Account of the Sensor Noise*, Sensors, vol. 20, no. 4, 1116 (2020), DOI: 10.3390/s20041116.

[20] Wajnert D., *A field-circuit model of the hybrid magnetic bearing*, Archive of Mechanical Engineering, vol. 66, no. 2, pp. 191–208 (2019), DOI: 10.24425/ame.2019.128444.